

Observations of Gravity Waves with High-Pass Filtering in the New Generation of Geostationary Imagers and Their Relation to Aircraft Turbulence

ANTHONY WIMMERS, SARAH GRIFFIN, JORDAN GERTH, SCOTT BACHMEIER, AND SCOTT LINDSTROM

Cooperative Institute for Meteorological Satellite Studies, University of Wisconsin–Madison, Madison, Wisconsin

(Manuscript received 22 June 2017, in final form 11 October 2017)

ABSTRACT

This paper introduces a method of image filtering for viewing gravity waves in satellite imagery, which is particularly timely to the advent of the next-generation Advanced Himawari Imager (AHI) and the Advanced Baseline Imager (ABI). Applying a “high pass” filter to the upper-troposphere water vapor channel reveals sub-Kelvin-degree variations in brightness temperature that depict an abundance of gravity wave activity at the AHI/ABI sensitivity. Three examples demonstrate that this high-pass product can be exploited in a forecasting setting to identify possible varieties of turbulence-prone gravity waves that either 1) move roughly orthogonally to the apparent background flow or 2) produce interference as separate wave packets pass through the same location.

1. Introduction

The higher resolution of the Advanced Himawari Imager (AHI) and the Advanced Baseline Imager (ABI) has been widely expected to improve the observation of gravity waves and, in turn, events leading to clear-air turbulence (CAT; e.g., Feltz et al. 2009). Improving near-real-time forecasting of CAT remains a high priority in the aviation community, with CAT being the leading cause of injury among commercial carriers and a cause of several fatalities for other aircraft in the United States (NASDAC 2004).

Gravity waves are known to be ubiquitous in the upper troposphere/lower stratosphere (UTLS) and are captured easily in high-resolution, nonhydrostatic numerical models with adequate spinup times. However, the global numerical weather prediction (NWP) models that are used operationally in the Pacific region, and even the regional models covering the continental United States, differ in their estimates of the intensity, location, and

character of gravity waves compared to satellite observations. Many NWP models also artificially dampen gravity waves for numerical stability. Most importantly, rapid convection is often poorly captured in near-real time by NWP models and can lead to significant aviation hazards in the surrounding area, whereas geostationary satellite imagery is very well suited to viewing these phenomena.

There are several causes of atmospheric disturbances that propagate through the atmosphere, often through gravity waves, that can lead to moderate or severe events of clear-air turbulence at aircraft cruising altitudes. These include topography (e.g., Lilly 1978), deep convection (e.g., Lane et al. 2003), frontal convergence (e.g., Trier and Sharman 2016), and jet-streak divergence (e.g., Koch et al. 2005). The state of the science, and especially the mechanisms that lead to turbulence, are summarized well in Sharman et al. (2012) and Plougonven and Zhang (2014, 2016). Of direct relevance here are any processes that transfer the energy of satellite-observed gravity waves into localized, smaller-scale turbulence. In broad terms, one general conception of turbulent flow applies to many scales, including the subpixel scale that is under the influence of observed gravity waves: flow becomes turbulent in areas of high horizontal/vertical shear and low static stability. This is most commonly expressed together in the gradient Richardson number (Ri; e.g., Miles 1986; Ellrod and Knapp 1992). Taken within this framework, turbulent conditions may arise from complex interactions of a gravity wave with its environment, as the variability

Denotes content that is immediately available upon publication as open access.

Supplemental information related to this paper is available at the Journals Online website: <https://doi.org/10.1175/WAF-D-17-0080.1>.

Corresponding author: Anthony Wimmers, wimmers@ssec.wisc.edu

DOI: 10.1175/WAF-D-17-0080.1

© 2018 American Meteorological Society. For information regarding reuse of this content and general copyright information, consult the AMS Copyright Policy (www.ametsoc.org/PUBSReuseLicenses).

of shear and stability within the wave can generate local regions of subcritical turbulent flow.

Within this picture of turbulence and its causes, we have begun to find types of gravity waves with consistent characteristics in the AHI/ABI water vapor channels that correspond to aircraft reports of turbulence. (However, only AHI observations will be presented here because at the time of writing only the AHI is in operational mode.) In our observations of AHI/ABI imagery, we have found a frequent association between aircraft turbulence and certain gravity wave characteristics shown in the following three examples, which may be significant to improving the process of operational turbulence forecasting and nowcasting. The purpose of this paper is to share a relevant method of image processing, and to show that even without a rigorous case study analysis, one can find simple visual cues in this new image product that indicate possible areas of CAT. Indeed, the examples shown here certainly have additional dynamical factors that contribute to turbulence such as anticyclonic flow and vertical shear, but here we will highlight only the image characteristics that forecasters can use to complement predictions of CAT from numerical models.

2. The 6.2- μm “water vapor” band

Our emphasis here is on the detection of gravity waves in the 6.2- μm (“upper-tropospheric water vapor”) band (or “channel”) and improving the identification of gravity waves that lead to aircraft turbulence. This band is the most relevant to long-range commercial aviation, because the sensitivity to water vapor enhances the signal of gravity waves, and the channel senses the highest layer of the atmosphere of the three water vapor channels. The full width at half maximum (FWHM) of the weighting function for band 8 is between 250 and 500 hPa, corresponding to 5.5–10.3 km or 18–34 kft in the standard atmosphere (Schmit et al. 2017). However, this serves as only a rough guide as to the height of gravity wave features in the imagery, for two reasons. First, the actual weighting function varies according to the vertical distribution of water vapor in the troposphere, so the actual layer being sensed can vary from the lower troposphere to the lower stratosphere. (However, the low brightness temperatures of the features analyzed in this study indicate signals mainly in the UTLS.) Second, a gravity wave signal in this imagery is not necessarily present in the whole layer sensed by the instrument. The variations in radiance caused by a wave could come from a thin layer within the sensed layer, or even a thick layer with only some vertical overlap with the sensed layer. Thus, in the following discussion we generally treat significant gravity wave features in this

AHI/ABI band as regions that are clearly relevant to aircraft at cruising altitude, rather than as regions with clearly defined altitudes.

3. High-pass filter

A fairly recent case of aircraft turbulence analysis inspired the development of the high-pass filter tool. On 14 December 2016 three wide-body aircraft recorded moderate-to-severe and severe turbulence between 35 and 38 kft (from 10.7 to 11.6 km) from 1530 to 1740 UTC in the mid-Pacific in the vicinity of an upper-level trough. One of the aircraft was equipped to measure and report the automated eddy dissipation rate (EDR), which is an objective, physical measurement of turbulence intensity (Sharman et al. 2014; Cornman 2017), and which directly locates the disturbance seen in satellite imagery (Fig. 1). An initial examination of the AHI band 8 imagery (upper-tropospheric water vapor channel) suggested gravity waves in the area, but the evidence was not clear (Fig. 1a). However, the imagery used then was the reduced-depth 8-bit imagery displayed with a default color map, which is the most common way to visualize this channel, and it did not show much color variation around the gravity wave feature. [Even more significantly, the NOAA/NCEP Advanced Weather Interactive Processing System (N-AWIPS) software still in use at some forecast offices displays this imagery at an even lower resolution of 6.5 bits per pixel.] In a reexamination using the full 11-bit imagery (Fig. 1b), the presence of gravity waves and their coincident timing with the turbulence event were clearly evident. The difference between the two images demonstrates that our existing display tools, which took shape in the GOES-I through GOES-P era, are often insufficient for revealing the full depth of information even from a single channel of the AHI or ABI. While a multi-color color map can just barely mark the 0.5-K brightness temperature variations in a channel’s natural range in the infrared, it will not distinguish the 0.1-K variations, which are quite relevant to gravity wave analysis.

On the other hand, analyzing gravity waves may require examining not the absolute image values, but rather only the *variations* in relative image value. To pursue this idea, we applied a high-pass filter (described below) as a way to isolate the signature of gravity waves in this example (Fig. 1c). In the resulting image, only the variations from -1 to $+1$ K from the local average are displayed, and a grayscale image of even a relatively low 8-bit depth can easily show the full range of gravity wave features. In addition, the animation of this figure (see Animation A in the online supplement to this paper) shows that the main gravity waves are moving to the east, while a second set of

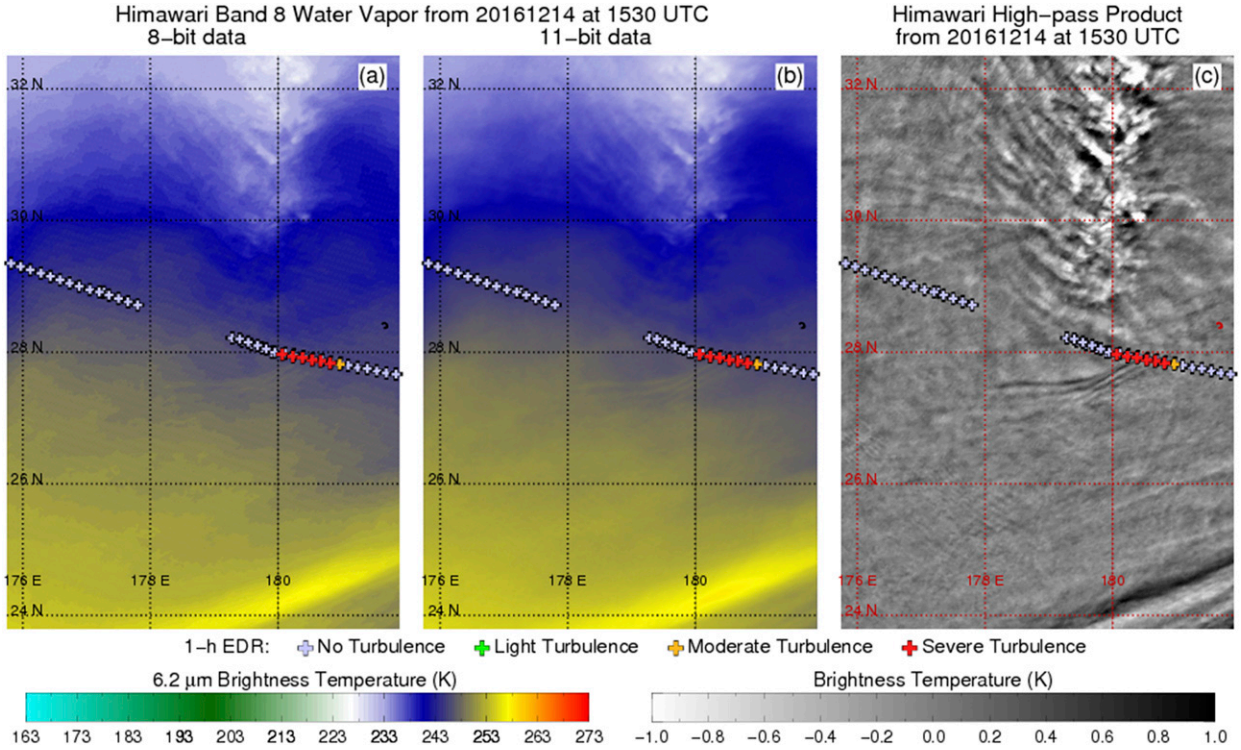


FIG. 1. Examples of the differences in gravity wave visualization between (a) a traditional 8-bit rendering of brightness temperature in the upper-level water vapor band, (b) a full 11-bit rendering, and (c) the high-pass product applied to the same data. Cross-shaped symbols along the flight track are automated EDRs (turbulence) peaking at $0.620 \text{ m}^{2/3} \text{ s}^{-1}$ (severe turbulence). Here and elsewhere, turbulence reports fall within 0–1 h before the image time. (See Animation A in the online supplement.)

south-propagating waves pass through the same location and possibly cause an interference pattern that leads to the turbulence. (In this case we did not use GFS wind fields to determine which of these wave patterns moved with or against the dominant flow, because the GFS winds and the evident motion of small cloud and water vapor features were not in agreement.)

The exact image filter used here is a Gaussian high-pass convolutional filter, although other related filter types can also perform well. The conventional representation of this formula is

$$I_{\text{hp}} = \text{HP}(\sigma) * I, \quad (1a)$$

where I is the initial image, I_{hp} is the filtered image, an asterisk (*) indicates the convolution of an image filter with an image, and $\text{HP}(\sigma)$ is the additive inverse of the Gaussian filter with width parameter σ :

$$\text{HP}(\sigma) = 1 - \frac{c}{\sigma\sqrt{2\pi}} \sum_{x,y} e^{-(x^2+y^2)/2\sigma^2}, \quad (1b)$$

where c is simply a constant that allows the weights to sum to unity. By design, this filter creates the exact opposite effect of a smoothing filter. That is, rather than

displaying the local averages of the image value, it shows the pixel's difference from the local average value. Thus, it can be calculated just as well as the difference between the original image and the product of a corresponding smoothing filter:

$$I_{\text{hp}} = I - G(\sigma) * I, \quad (1c)$$

where $G(\sigma)$ is the Gaussian filter with width parameter σ . This is often an easier way to present the high-pass filter to audiences already familiar with smoothing filters. In the examples here we use $\sigma = 5$ pixels (10 km at nadir, or 14 km at a zenith angle of 45°).

As a convolutional filter, the algorithm can process an entire AHI image in less than a second because of the computational efficiency of the fast Fourier transform. Another benefit is that the low bit depth of the derived product makes it easier to transmit, display, and also overlay related data such as manual and automated pilot reports.

4. Comparison to GOES-15

The improvement in resolution (spatial, temporal, and radiance) of the AHI/ABI over the previous generation of MTSAT and GOES-N series imagers of

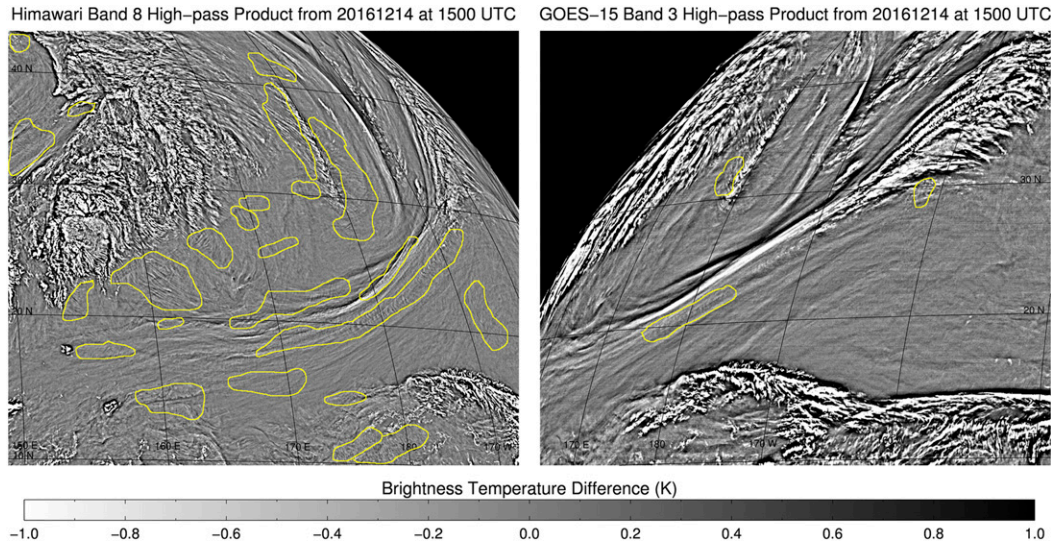


FIG. 2. Areas of cloud-free or nearly cloud-free gravity waves identified by inspection (yellow) from the high-pass products of (left) *Himawari-8* AHI band 8 and (right) *GOES-15* Imager band 3.

course leads to a general increase in detail. This is especially clear in a comparison of high-pass-filtered imagery of AHI band 8 and *GOES-15* band 3 (the upper-tropospheric water vapor channels) (Fig. 2). The 0.1-K, 2-km (nadir) resolution from AHI reveals a ubiquity of gravity waves across the Pacific, whereas the 0.5-K, 4-km (nadir) resolution of *GOES-15* is generally too coarse for this scale of activity. Only a few small gravity wave features can be identified in the *GOES-15* image, and even

those may be too subtle to receive notice from a forecaster. This may explain why the concept of high-pass filtering has not been introduced as a forecasting tool until now. Furthermore, while polar-orbiting satellite instruments such as MODIS had adequate resolution for a similar analysis (e.g., Uhlenbrock et al. 2007), the imagery was not suited for real-time forecasting and would not have experienced the same push for a new kind of image visualization.

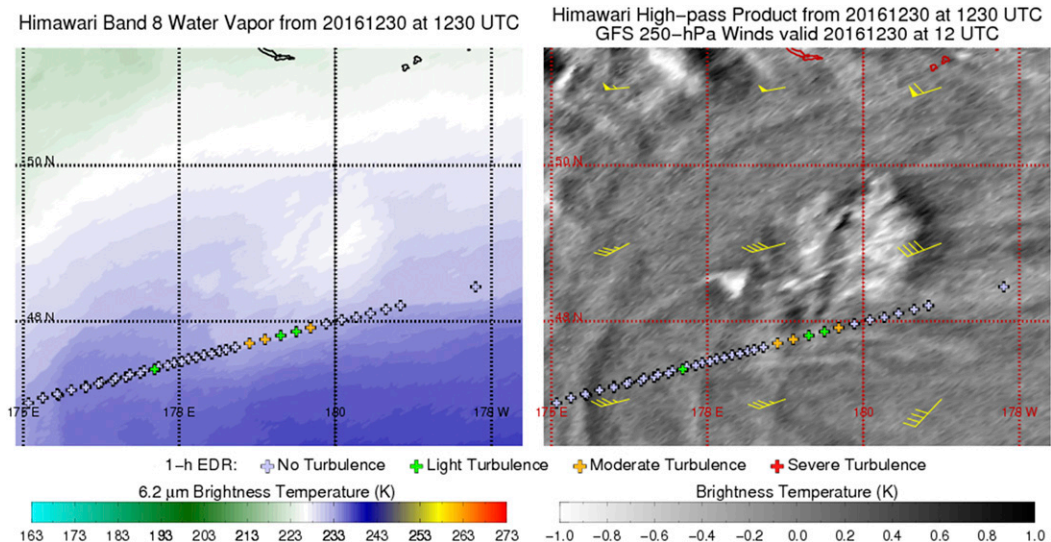


FIG. 3. Example of convectively induced gravity waves leading to moderate aircraft turbulence. (left) While the convective cell can be seen in the band 8 brightness temperature, the gravity waves are not apparent. (right) In the high-pass product, gravity waves appear as bright east–west-oriented bands from 178°E to beyond 180°. In Animation B in the online supplement, the bands are seen propagating to the south amid a background wind from the WSW, shown here in the GFS 250-hPa analysis winds (yellow barbs).

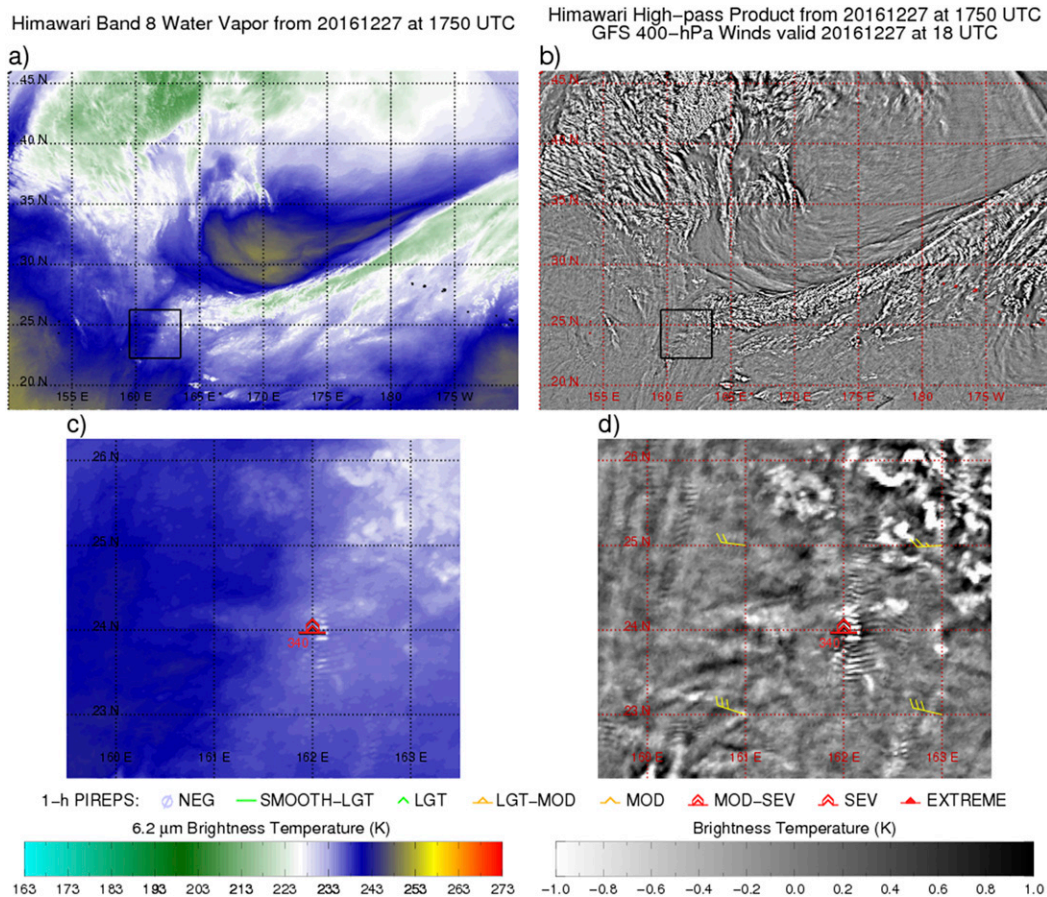


FIG. 4. Example of enhanced viewing of gravity waves in a turbulent environment. (a),(b) The larger context of the event in the mid-Pacific, and (c),(d) the gravity wave activity can be seen to extend over a wider area using the high-pass product. A moderate-to-severe (MOD-SEV) pilot report (red) at 34 kft (10.4 km) in elevation is coincident with the highest-amplitude section of the waves. The GFS analysis winds (yellow barbs) show that the gravity wave propagation is roughly orthogonal to the dominant flow in the image. (See Animation C in the online supplement.)

5. Additional observations of gravity wave-related aircraft turbulence

With such an abundance of gravity wave activity suddenly in view in a geostationary image, the new challenge for forecasters is no longer where to find gravity waves because of their potential for turbulence, but rather how to distinguish turbulence-generating gravity waves from more common, benign gravity waves. Two additional cases here further highlight a method of identifying at least one subset of gravity waves that may have a higher likelihood of generating aircraft turbulence.

The first case is an event of convectively induced turbulence in the mid-Pacific on 30 December 2016 (Fig. 3; see also Animation B in the online supplement). Gravity waves are seen to propagate southward starting at the time of a convective cell’s most rapid growth around 1100 UTC at 48°N, 179°E. Meanwhile, the background flow at this level remains from the west-southwest (where in this

context “background flow” describes the direction of the dominate shapes and textures in the imagery). In this case the background flow corresponds to the GFS winds at 250 hPa. On encountering the gravity wave, a Boeing 767 aircraft recorded EDRs peaking at $0.300 \text{ m}^{2/3} \text{ s}^{-1}$ at 36 kft (10.9 km), corresponding to moderate turbulence (Sharman et al. 2014).

The second case involves more unique-looking gravity waves in the west Pacific on 27 December 2016 (Fig. 4; see also Animation C in the online supplement). While the background flow at 400 hPa is from the west-northwest along the southern end of a frontal boundary, a collection of thin gravity wave packets propagates to the south. Some of the features are evident in the high color contrast brightness temperature image, but the full extent of the phenomenon is only clear in the high-pass-filter product. As noted in Fig. 4, a moderate-to-severe pilot report occurred at one of the more pronounced wave features.

In both of these cases the gravity waves do not propagate in the direction of the background flow, rather they propagate roughly orthogonally to the background flow. We can offer a few possible explanations for the enhanced turbulence in the vicinity of these waves. First, if the gravity waves are located within convective outflow, the outflow region would likely have significant vertical shear contributing to a low Ri. Gravity waves could create local regions of critically low Ri. This is important within the context of nowcasting, because the exact location of the convection and outflow may not be well captured in an NWP model. In a related sense, any highly vertically sheared flow not captured in an NWP model can have this same tendency toward low Ri that is indicated only by satellite. Second, the heterogeneity or the outside edges of a wave packet could induce complicated, unstable interactions with the surrounding flow. And third, interaction between separate gravity wave packets is more likely in these regions of directional shear, increasing the chances of subcritical flow. This is suggested by the juxtaposition of waves in the 14 December case seen in Animation A in the online supplement. Furthermore, these three factors may also occur in combination, as they are not mutually exclusive.

6. Conclusions

High-pass filtering of water vapor channels in the new generation of geostationary imagers can more easily and directly depict the small-scale fluctuations in brightness temperature that many forecasters particularly wish to examine, and the natural focus for this capability is the observation of gravity waves. The examples shown here are an initial demonstration of both the observation of gravity waves and a description of the patterns of motion that can be used to improve the nowcasting/forecasting of aviation turbulence. This is another circumstance in which geostationary satellite imagery plays an essential forecasting role of verifying, enhancing, and correcting predictions from numerical models. With further work we may be able to refine and generalize these observations into a set of forecasting best practices and, afterward, into automated techniques that identify hazards with proper lead times.

Acknowledgments. The authors thank Tom Fahey and Bill Watts, from Delta Air Lines, and Tim Rahmes, from Boeing, for their assistance with the automated aircraft weather and turbulence (EDR) observations. Three anonymous reviewers also significantly improved the quality of this manuscript. This work is funded under NOAA Award NA15NES4320001 (GOES-R Risk Reduction Program—Turbulence initiative).

REFERENCES

- Cornman, L. B., 2017: Airborne in situ measurements of turbulence. *Aviation Turbulence: Processes, Detection, and Prediction*, R. D. Sharman and T. P. Lane, Eds., Springer, 97–120.
- Ellrod, G. P., and D. L. Knapp, 1992: An objective clear-air turbulence forecasting technique: Verification and operational use. *Wea. Forecasting*, **7**, 150–165, [https://doi.org/10.1175/1520-0434\(1992\)007<0150:AOCATF>2.0.CO;2](https://doi.org/10.1175/1520-0434(1992)007<0150:AOCATF>2.0.CO;2).
- Feltz, W. F., K. M. Bedka, J. A. Otkin, T. Greenwald, and S. A. Ackerman, 2009: Understanding satellite-observed mountain-wave signatures using high-resolution numerical model data. *Wea. Forecasting*, **24**, 76–86, <https://doi.org/10.1175/2008WAF2222127.1>.
- Koch, S. E., and Coauthors, 2005: Turbulence and gravity waves within an upper-level front. *J. Atmos. Sci.*, **62**, 3885–3908, <https://doi.org/10.1175/JAS3574.1>.
- Lane, T. P., R. D. Sharman, T. L. Clark, and H.-M. Hsu, 2003: An investigation of turbulence generation mechanisms above deep convection. *J. Atmos. Sci.*, **60**, 1297–1321, [https://doi.org/10.1175/1520-0469\(2003\)60<1297:AIOTGM>2.0.CO;2](https://doi.org/10.1175/1520-0469(2003)60<1297:AIOTGM>2.0.CO;2).
- Lilly, D. K., 1978: A severe downslope windstorm and aircraft turbulence event induced by a mountain wave. *J. Atmos. Sci.*, **35**, 59–77, [https://doi.org/10.1175/1520-0469\(1978\)035<0059:ASDWAA>2.0.CO;2](https://doi.org/10.1175/1520-0469(1978)035<0059:ASDWAA>2.0.CO;2).
- Miles, J., 1986: Richardson's criterion for the stability of stratified shear flow. *Phys. Fluids*, **29**, 13 049–13 062, <https://doi.org/10.1063/1.865812>.
- NASDAC, 2004: Review of aviation accidents involving weather turbulence in the United States: 1992–2001. National Aviation Safety Data Analysis Center Ref. 04-551, 22 pp., http://www.asias.faa.gov/i/turbulence_study_new.pdf.
- Plougonven, R., and F. Zhang, 2014: Internal gravity waves from jets and fronts. *Rev. Geophys.*, **52**, 33–76, <https://doi.org/10.1002/2012RG000419>.
- , and —, 2016: Gravity waves generated by jets and fronts and their relevance for clear-air turbulence. *Aviation Turbulence: Processes, Detection, and Prediction*, R. D. Sharman and T. P. Lane, Eds., Springer, 385–406.
- Schmit, T. J., P. Griffith, M. M. Gunshor, J. M. Daniels, S. J. Goodman, and W. J. Lebar, 2017: A closer look at the ABI on the GOES-R series. *Bull. Amer. Meteor. Soc.*, **98**, 681–698, <https://doi.org/10.1175/BAMS-D-15-00230.1>.
- Sharman, R. D., S. B. Trier, T. P. Lane, and J. D. Doyle, 2012: Sources and dynamics of turbulence in the upper troposphere and lower stratosphere: A review. *Geophys. Res. Lett.*, **39**, L12803, <https://doi.org/10.1029/2012GL051996>.
- , L. B. Cornman, G. Meymaris, J. Pearson, and T. Farrar, 2014: Description and derived climatologies of automated in situ eddy-dissipation-rate reports of atmospheric turbulence. *J. Appl. Meteor. Climatol.*, **53**, 1416–1432, <https://doi.org/10.1175/JAMC-D-13-0329.1>.
- Trier, S. B., and R. D. Sharman, 2016: Mechanisms influencing cirrus banding and aviation turbulence near a convectively enhanced upper-level jet stream. *Mon. Wea. Rev.*, **144**, 3003–3027, <https://doi.org/10.1175/MWR-D-16-0094.1>.
- Uhlenbrock, N. L., K. M. Bedka, W. F. Feltz, and S. A. Ackerman, 2007: Mountain wave signatures in MODIS 6.7- μm imagery and their relation to pilot reports of turbulence. *Wea. Forecasting*, **22**, 662–670, <https://doi.org/10.1175/WAF1007.1>.